Heliyon 8 (2022) e12397

Contents lists available at ScienceDirect

Heliyon

journal homepage: www.cell.com/heliyon

Research article

# A parametric metamodel of the vehicle frontal structure accounting for material properties and strain-rate effect: application to full frontal rigid barrier crash test

Angelo Pasquale [a,c,*,1], Victor Champaney [a,1], Youngtae Kim [b], Nicolas Hascoët [a], Amine Ammar [c], Francisco Chinesta [a,d]

[a] ESI Group Chair @ PIMM Lab, ENSAM Institute of Technology, 151 Boulevard de l'Hôpital, F-75013, Paris, France
[b] Hyundai Motor Group, Virtual Technology Innovation Research Lab, Automotive R&D Division, 150 HyundaiYeonguso-ro, Namyang-eup, Hwaseong-si, Gyeonggi-do, 18280, Republic of Korea
[c] ESI Group Chair @ LAMPA Lab, ENSAM Institute of Technology, 2 Boulevard du Ronceray BP 93525, 49035 Angers cedex 01, France
[d] ESI Group, Parc Icade, Immeuble le Seville, 3 bis, Saarinen, 94528, Rungis Cedex, France

ARTICLE INFO

*Keywords:*
MOR
sPGD
Multi-sPGD
PODI
Curves metamodeling
Vehicle frontal structure
Crashworthiness
Lightweightness
Parametric strain-hardening laws

ABSTRACT

In the automotive industry, building parametric surrogate models is a fundamental tool to evaluate, in real time, the performance of newly designed car components. Such models allow to compute any Quantity of Interest —QoI—, such as a specific safety protocol index, for any choice of material and/or geometrical parameters characterizing the component, within the stringent real time constraint. For instance, they can be exploited to guarantee safer designs (e.g., maximizing energy absorption by the crash boxes) or to reduce manufacturing costs (e.g., minimizing the mass of a specific structure under some safety protocol constraints). In general, these parametric simulation tools allow a significant gain in terms of manufacturing costs and time delays during the investigation phase. In this study, we focus on the vehicle frontal structure system considering its performance in a full-frontal crash scenario. In the front structure system we parameterize the crash boxes (left and right) and the inner/outer side front members (left and right, front and rear) with respect to the part thickness and the material parameters characterizing the Krupkowski plasticity curve. Moreover, Strain Rate Effect is also taken into account via Neural Network based regressions, whose training dataset comes from experimental data. The parametric metamodel is built via Non-Intrusive PGD —NI–PGD— strategies, relying on a sparse sampling of the parametric space, and allowing a quite reduced number of High Fidelity —HiFi— simulations. A novel strategy based on clustering and classification, known as Multi-PGD, is also applied and numerically verified.

## 1. Introduction

In this paper, we revisit some state-of-the-art Model Order Reduction —MOR— technologies and propose new advances to address safety analyses in the automotive industry.[2] The main goal of the work is to build a parametric metamodel of the vehicle frontal structure (involving material properties and design parameters), enabling accurate real-time evaluations of its response to a crash scenario. Such model allows fast optimization, inverse analysis and uncertainty propagation; it can be exploited, for instance, to guarantee safer designs (e.g., maximizing energy absorption by the crash boxes) or to reduce manufacturing costs (e.g., minimizing the mass of a specific structure under some safety protocol constraints).

MOR is a really wide topic, largely covered in the existing literature [1, 2, 3]. This work primarily focuses on snapshots-based reduced-order modeling (a subject that is extensively discussed in [2]) and, particularly, on the Proper Orthogonal Decomposition —POD— and on the sparse Proper Generalized Decomposition —sPGD—. Extensive reviews

* Corresponding author at: ESI Group Chair @ PIMM Lab, ENSAM Institute of Technology, 151 Boulevard de l'Hôpital, F-75013, Paris, France.
*E-mail address:* angelo.pasquale@ensam.eu (A. Pasquale).
[1] These authors equally contributed.
[2] The work is developed in collaboration with Hyundai Motor Company, in the context of the International Research Chair CREATE-ID between ESI Group and ENSAM ParisTech.

https://doi.org/10.1016/j.heliyon.2022.e12397
Received 19 July 2022; Received in revised form 28 September 2022; Accepted 8 December 2022

2405-8440/© 2022 The Authors. Published by Elsevier Ltd. This is an open access article under the CC BY license (http://creativecommons.org/licenses/by/4.0/).

and investigations on such techniques can be found in [4, 5, 6, 7, 8, 9, 10, 11, 12]. In particular, in the recent work [10], the authors deal with parametric metamodeling of curves, based on POD, PGD, data alignment, data clustering and data classification, with emphasis in computational materials science. Moreover, in [10], authors exploit the surrogates to quantify and propagate uncertainty, obtaining parametric statistical bounds for the predicted curves. This paper follows and further develops the methods introduced in [10], focusing in particular on the study-case of vehicle crash simulations. Within such context, even though similar workflows have already been applied in literature (e.g., [13, 14, 15]), this work presents elements of novelty both from the viewpoint of the applied methodologies and from the analyzed model features. In terms of methodologies, the multi-sPGD is applied, combining the sPGD regression with clustering and classification algorithms based on crash modes. The main motivation beyond the choice of the method is that the sPGD allows the usage of a reduced number of offline simulations (which are highly expensive computationally when the full vehicle is considered). This is not trivial when working in high-dimensional spaces and with highly non-linear problems, which is the case studied in this work. Moreover, the combination of the sPGD with clustering and classification is an innovative sub-modeling procedure allowing to improve the model accuracy. In terms of model features, we focus on the vehicle frontal structure, whose thicknesses and materials' Krupkowski strain-hardening laws are parametric (for a total number of 13 parameters). A standard sampling strategy based on Latin-Hypercube Sampling —LHS— to select the Krupkowski parameters would not have allowed physical-consistent results. For this reason, a specific sampling based on physical materials' properties has been employed, representing another innovative part of the work. Particularly, this makes use of the $k$-nearest neighbors algorithm (alternatives would be manifold learning techniques) to move close to the manifold of experimental data (existing and tested materials). Moreover, another point of novelty is the usage of Neural Networks (trained on experimental data) to account for strain-dependent plasticity in the metamodel.

The sPGD regression is employed following the methods widely detailed in Section 2 of [10]. More specifically, the approximation of curves is performed within a POD-based approach (Subsection 2.3.3.1 of [10]) and a quality enhancement of the regression is achieved through a clustering-classification strategy (Subsection 2.4 of [10]).

Since works such as [8, 10] extensively expose all the specifics of the methods, hereafter we only briefly go over the sPGD method's core concept.

For the sake of simplicity and without loss of generality, we consider function $u(x, y)$, with $x$ and $y$ two parameters defined in $\Omega \subset \mathbb{R}^2$. We look for the approximate $u^M(x, y)$ expressed in the separated form given in Eq. (1)

$$u^M(x,y) = \sum_{m=1}^{M} X_m(x) \cdot Y_m(y) = \sum_{m=1}^{M} (\mathbf{N}_m^{x^T}(x)\mathbf{a}_m^x) \cdot (\mathbf{N}_m^{y^T}(y)\mathbf{a}_m^y), \tag{1}$$

where $M$ refers the number of terms (rank) of the finite sum decomposition, vectors $\mathbf{N}_m^x(x)$ and $\mathbf{N}_m^y(y)$ contain the functions involved in the approximation of $X_m(x)$ and $Y_m(y)$ respectively, and $\mathbf{a}_m^x$ and $\mathbf{a}_m^y$ contain the associated (searched) coefficients.

With the first $M-1$ modes already calculated, the obtention of the $M$-mode results from the minimization problem

$$(\mathbf{N}_M^{x^T}(x)\mathbf{a}_M^x) \cdot (\mathbf{N}_M^{y^T}(y)\mathbf{a}_M^y) = \arg\min_{\mathbf{a}_M^{x*}, \mathbf{a}_M^{y*}} \sum_{i=1}^{D} \left| u(x_i, y_i) - u^{M-1}(x_i, y_i) + (\mathbf{N}_M^{x^T}(x_i)\mathbf{a}_M^{x*}) \cdot (\mathbf{N}_M^{y^T}(y_i)\mathbf{a}_M^{y*}) \right|^2, \tag{2}$$

where $D$ is the number of available data-points, $(x_i, y_i)$, $i = 1, \ldots, D$, for which the solution is assumed known (high-fidelity solutions) $u(x_i, y_i)$.

Eq. (2) proceeds by calculating iteratively coefficients $\mathbf{a}_m^x$ and $\mathbf{a}_m^y$, from Eq. (3) and (4), respectively

$$\left\| \mathbf{K}_M^x \mathbf{a}_M^x - \mathbf{r} \right\|^2, \tag{3}$$

$$\left\| \mathbf{K}_M^y \mathbf{a}_M^y - \mathbf{r} \right\|^2, \tag{4}$$

both solved in a least square sense, with $\mathbf{K}_M^x$, $\mathbf{K}_M^x$ and $\mathbf{r}$ derived from Eq. (2).

To avoid overfitting the richness of the approximation bases used at each level ($m$) is controlled, by increasing gradually the approximation degree when increasing $m$.

The paper is structured as follows. In Section 2 the target system is presented, describing in detail the parametric vehicle frontal structure. Section 3 represents an introductory example to the sPGD based regression within the PODI MOR builder; only the thicknesses are considered in this case. Section 4 describes in detail the integration of material properties and strain-rate dependent Krupkowski plasticity into the sPGD model. Section 5 presents the multi-PGD approach based on clustering different crash dynamics. Section 4 and 5 represent the main original contributions of this work. Section 6 is a short conclusion on the proposed method and discusses several industrial applications.

## 2. Target system

The vehicle front structure composed by the crash boxes, the front side inner members (front and rear) and the front side outer member is parametrized. The target system is shown in Fig. 1, while Fig. 2 gives multiple zoomed views of the parametric parts.

Numerical simulations of the vehicle full-frontal rigid barrier crash are carried-out using the finite element method with the commercial software LS-Dyna used by Hyundai. The frontal structure is discretized by means of 23233 shell elements (23737 nodes), as shown in Fig. 3, and using 5 integration points through-the-thickness. The mesh of the full vehicle consists of several millions of elements (solids, beam and thin shell types) and has been verified being fine enough to ensure accurate high-fidelity simulations. Moreover, we stress the fact that the quality of the parametric model is evaluated with respect to LS-Dyna simulations, and not with respect to the experimental tests of the full-car crash test. This because, as usually done in reduced-order modeling, the target is the solution we would obtain by performing the full-order simulation.

Quantities of interest are extracted at the measurement nodes located at the bottom of the B-pillar (left and right), as shown in Fig. 4. Particularly, we focus on displacement, velocity and acceleration along the $x$-direction. The crash pulse curve (acceleration time history) is obtained by deriving the velocity signal computed by LS-Dyna and then filtering according to the CFC60 filter class (based on the iso6487 standard).

The initial velocity of the vehicle is approximately 55 km/h and a full frontal rigid barrier crash is simulated over the first 100 ms. Acceleration is measured in standard gravity $g$. Fig. 5 shows the deformation behavior of the parts of interest.

Some important crash severity parameters are listed here below:

- The 1st peak of acceleration curve is defined as the maximum value of the filtered acceleration curve over the first 27 ms. The upper-bound of this safety index is a peak value of 25 $g$.
- The Occupant Load Criterion —OLC— which indicates the minimum occupant acceleration, induced by a given crash pulse under the protection of the ideal restraint system [16, 17, 18]. When the occupant reaches the distance of 65 mm, it is assumed that the occupant is optimally restrained. The EuroNCAP procedure for the computation of OLC is detailed in [19] and described here below:
  1. let $v_0$ and $v$ denote $x$-velocity at initial time $t_0$ and a generic time $t$, respectively;
  2. let $S_1(t) = \int_0^t (v_0 - v)\,\mathrm{d}t$;
  3. find the time $t_2$ such that $S_1(t_2) = 65$ mm;
  4. define $S_2(t) = (t - t_2)(v_0 - v)/2$;
  5. find the time $t_3$ such that $S_2(t_3) - S_1(t_3) = 300$ mm;
  6. use the definition $\mathrm{OLC} = -\frac{v(t_3) - v(t_2)}{t_3 - t_2}$.

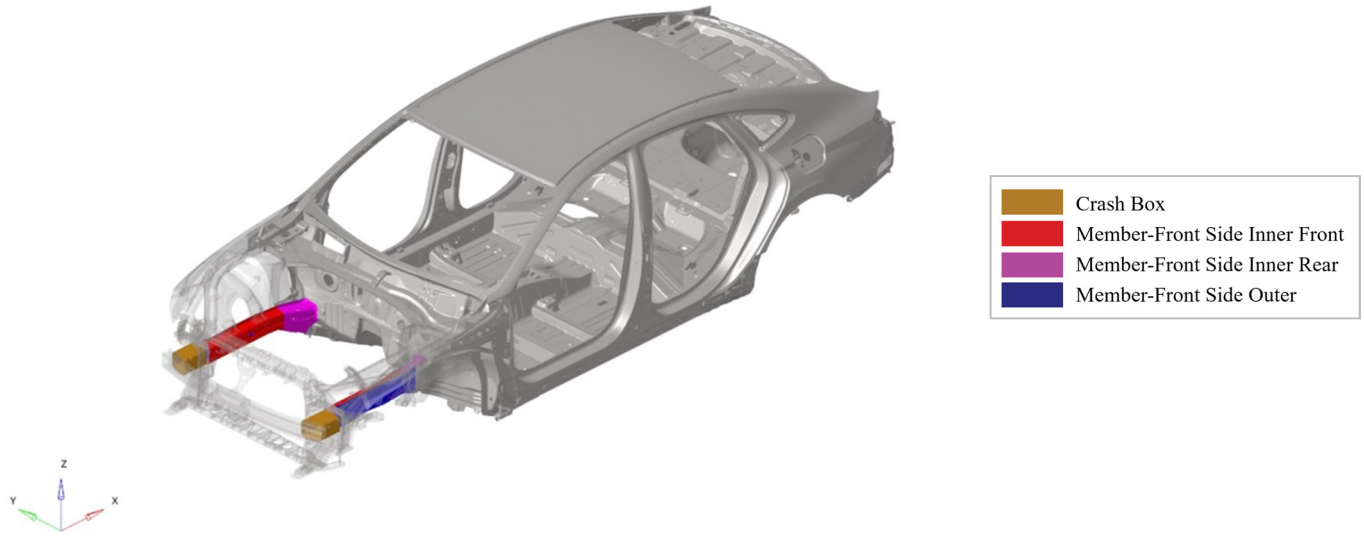
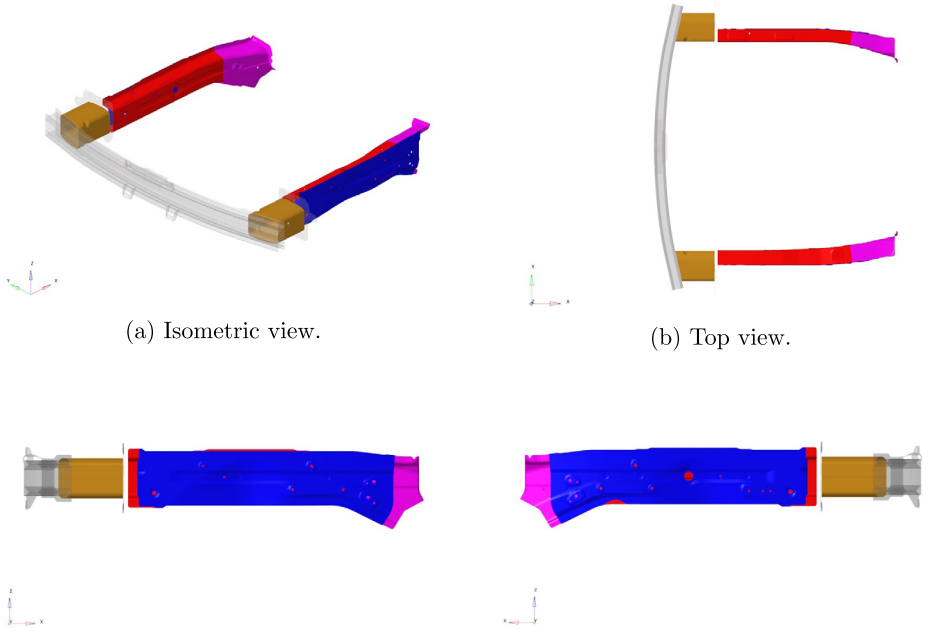



**Fig. 1.** Full car model and highlighted target system.



(a) Isometric view. (b) Top view.

(c) Left view. (d) Right view.

**Fig. 2.** Zoom of the target system.

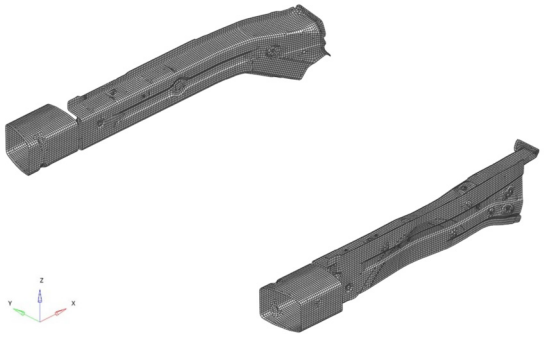


**Fig. 3.** Mesh of the target system.

Values in between 30 g and 35 g are considered as an acceptable crash performance in our study.

- The Ride-Down Energy —RDE— computed by taking the integral of the acceleration-displacement curve $a$-$x$. Detailed analysis for ride-down mechanism can be found in [20, 21, 22, 23]. The concept of ride-down efficient and the ride-down existent criteria are discussed in [20, 23]. Denoting with $E_{\text{rd}}$ the ride-down energy density and with $E$ the initial occupant kinetic energy density (assuming for the occupant the same velocity as the impact speed), then the ride-down energy density rate is defined as $R_{\text{rd}} = E_{\text{rd}}/E$ and we consider the occupant injury to be acceptable for rate values under $< 50\%$.
- The rebound time, that is the time instant in which the velocity curve gets to zero.

## 3. Parametric model with part thicknesses

For the sake of methodological illustration, we first build a parametric model considering only the part thicknesses. Table 1 summarizes the

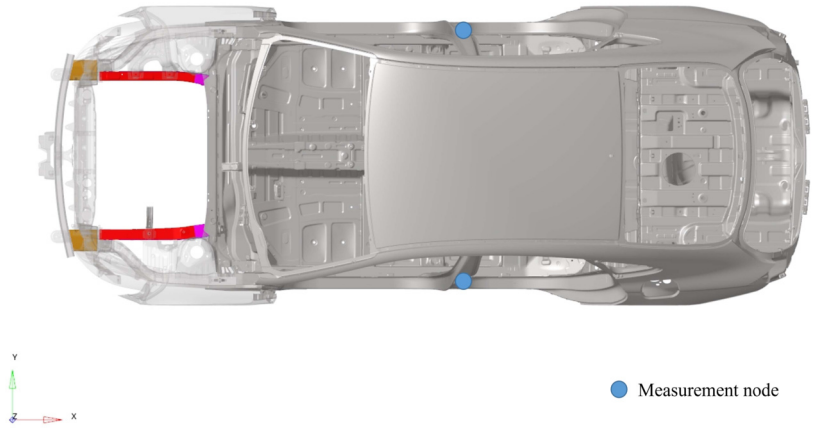



**Fig. 4.** Location of measurement nodes (LH/RH).

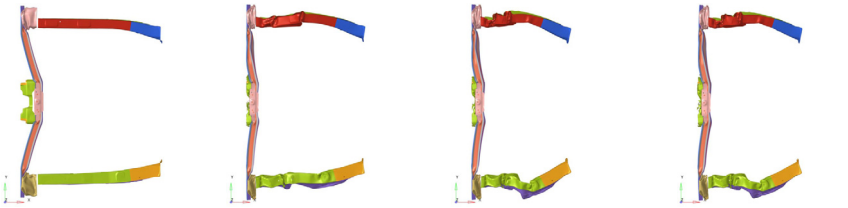



**Fig. 5.** Deformation behavior evolving in time during crash.

**Table 1**. Thickness information.

| Part (LH/RH) | Original Thickness [mm] | Parameter Range [mm] |
|---|---|---|
| Member-Front Side Outer | 1.4 | $t_1 \in [0.8, 2.3]$ |
| Member-Front Side Inner Front | 1.8 | $t_2 \in [0.8, 2.3]$ |
| Member-Front Side Inner Rear | 2 | $t_3 \in [0.8, 2.3]$ |
| Crash Box | 3.2 | $t_4 \in [2, 4]$ |

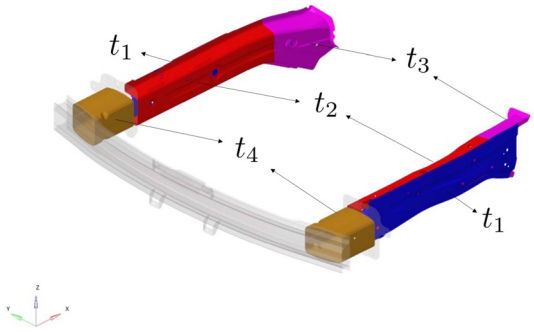



**Fig. 6.** Sketch of parts with parametric thickness.

original thickness of parts of interest as well as the parametric ranges covered by the model of the frontal structure, sketched in Fig. 6.

10 High-Fidelity simulations are chosen by means of a Latin Hypercube Sampling. The sampled points in the parametric space are reported in Table 2.

In Fig. 7, we give the plots of the displacement and velocity curves obtained by integration of the filtered acceleration. The sub-figures at top and bottom are related to left-hand (LH) and right-hand (RH) side measurement node, respectively (as shown in Fig. 4). Moreover the negative sign is related to the fixed reference system and chosen positive direction.

Following the procedure described in Section 2 of [10], a POD basis is extracted from 8 Hi-Fi simulations, while remaining 2 (run 3 and run 8) are taken for testing. Analyzing the singular values pattern, we deduce that two modes contain the most information. For instance, Figs. 8 and 9 show the POD results in the case of displacement and velocity computed at the left-side of the vehicle (LH), respectively. A basis of quite few time modes (two in this example) is thus retrieved employing the truncated POD and, then, the sPGD method is applied to predict the coefficients (weights) of such modes. Once the model has been trained and calibrated, new coefficients can be predicted for a novel choice of parameters and time functions are reconstructed using the reduced POD basis.

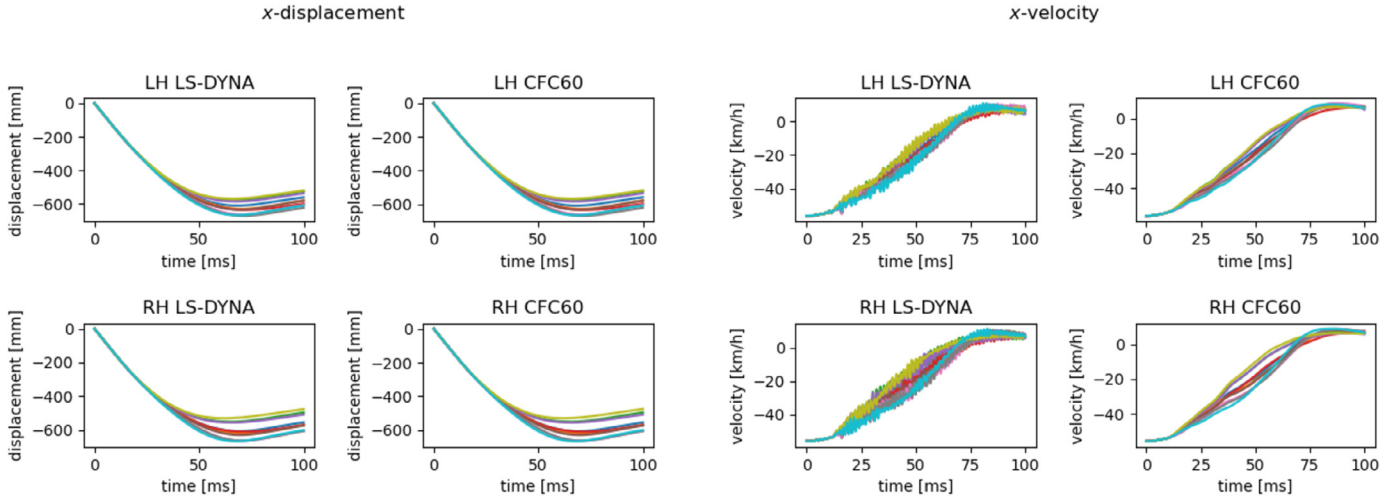
**Table 2**. DoE for thickness (data in mm).

| Run | $t_1$ | $t_2$ | $t_3$ | $t_4$ |
|---|---|---|---|---|
| 1 | 1.080 | 1.689 | 1.927 | 2.426 |
| 2 | 2.020 | 1.364 | 1.499 | 3.583 |
| 3 | 1.763 | 1.832 | 2.165 | 3.320 |
| 4 | 0.868 | 1.972 | 1.045 | 2.748 |
| 5 | 1.678 | 2.114 | 1.383 | 3.040 |
| 6 | 1.122 | 1.487 | 1.133 | 2.314 |
| 7 | 2.207 | 0.943 | 2.092 | 2.018 |
| 8 | 1.497 | 1.115 | 0.914 | 2.964 |
| 9 | 1.923 | 2.158 | 1.639 | 3.747 |
| 10 | 1.340 | 1.026 | 1.836 | 3.971 |

Figs. 10 and 11 show the results on the test runs, for the displacement and velocity respectively. Both the results show great accuracy.

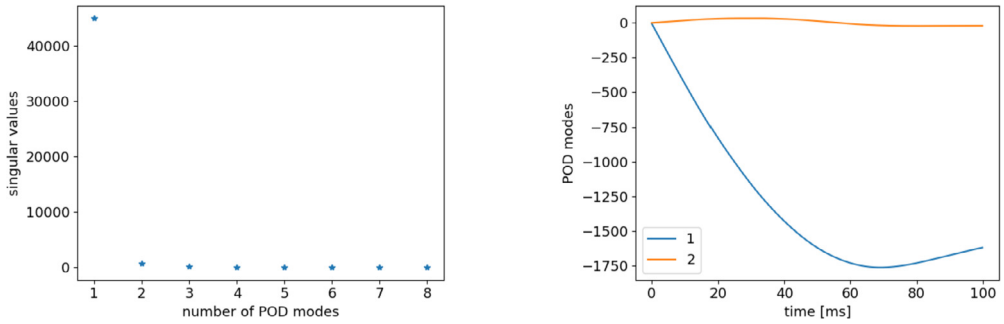
## 4. Accounting for material properties

The core of the work is considering material properties in the metamodel. With the aim of simulating virtual plastic materials, a Krupkowski strain-hardening law is considered, as usual in the high-fidelity models. For this to be done, two important novelties are introduced. The first one concerns the Design of Experiments —DoE— and, particularly, a physics-informed sampling strategy following the manifolds experimentally observed. The second one is related to the strain-dependent plasticity accounted by using Neural Networks, respecting the static and dynamic tests experimentally performed over materials specimens. These points are explained in detail hereafter.



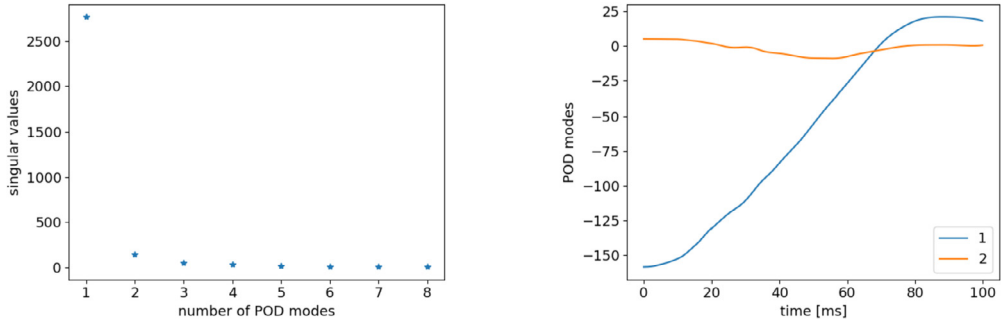

(a) Filtered displacement. (b) Filtered velocity.

**Fig. 7.** Filtered curves for 10 runs of Table 2 (LH and RH measurement points at top and bottom, respectively).




(a) Decay of singular values. (b) Selected modes.

**Fig. 8.** POD results for LH $x$-displacement snapshots.




(a) Decay of singular values. (b) Selected modes.

**Fig. 9.** POD results for LH $x$-velocity snapshots.

### 4.1. Sampling strategy

In this study, the material properties of the front side members (steel parts) are also considered as problem parameters. For each part, we consider the 3 parameters $(n, K, \varepsilon_0)$ characterizing the Krupkowski strain-hardening law

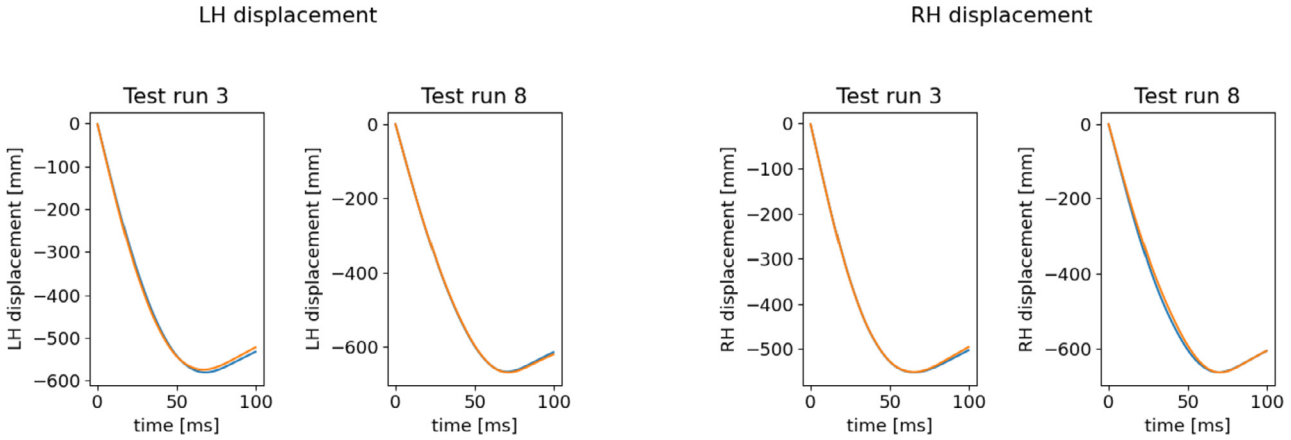
$$\sigma = K(\varepsilon + \varepsilon_0)^n,$$

linking the True Strength and the True Strain.

Since a Latin Hypercube Sampling —LHS— for the point $(n, K, \varepsilon_0)$ could lead to nonphysical results, we perform the sampling over three physical properties: the Yield Strength YS ($R_p$), the Ultimate Tensile Strength UTS ($R_m$) and the Uniform Elongation U-El ($A_g$, in %). Fig. 12 shows the location of such points over a typical plasticity curve linking the Engineering Strength and Engineering Strain.

From the sampled tuple (YS, UTS, U-El), we compute the corresponding Krupkowski parameters $(K, n, \varepsilon_0)$ by means of a non-linear optimization algorithm, detailed hereafter (Algorithm 1). Once such parameters are computed, the Krupkowski plasticity curve $(\varepsilon, \sigma)$ identifies the material of a specific part.

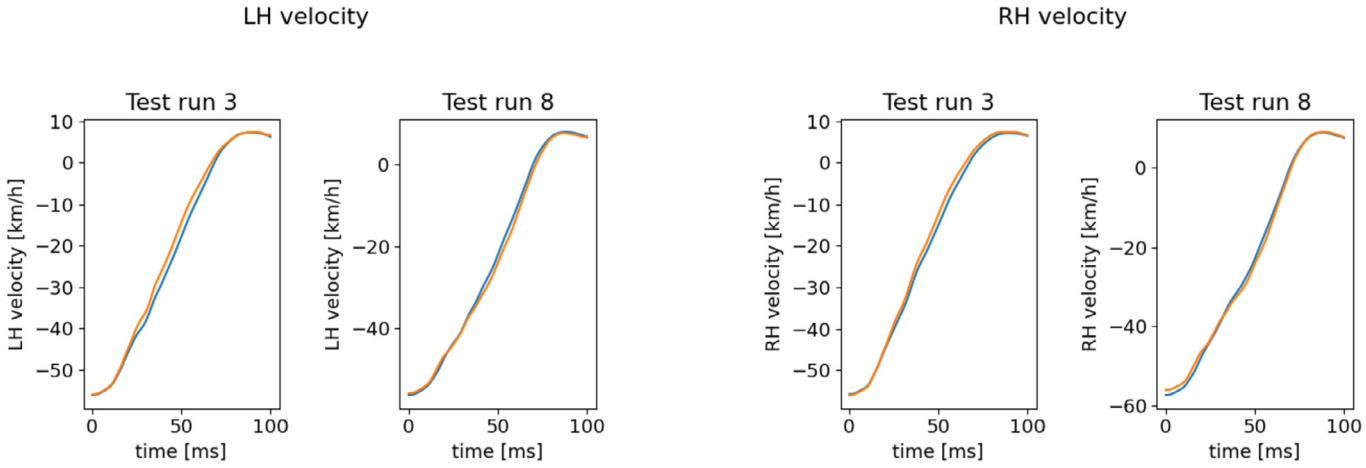
As one can deduce from Fig. 12, the sampling of material properties shall also meet some requirements to ensure realistic plastic behaviors. For instance, if values of $R_m$ and $R_p$ are too close, then the fitted curve would be meaningless (perfect plasticity). To avoid such uncomfortable




(a) Displacement at LH measurement point.

(b) Displacement at RH measurement point.

**Fig. 10.** Reconstructed $x$-displacement using the sPGD models (orange: Hi-Fi simulation, blue: Reduced Model).




(a) Velocity at LH measurement point.

(b) Velocity at RH measurement point.

**Fig. 11.** Reconstructed $x$-velocity using the sPGD models (orange: Hi-Fi simulation, blue: Reduced Model).

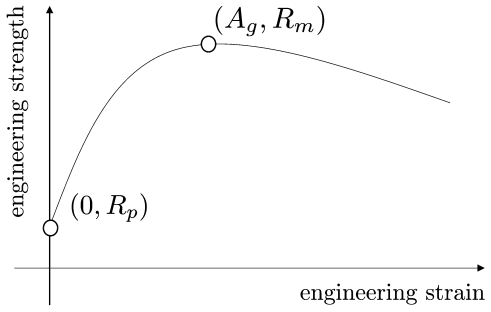



**Fig. 12.** Plasticity curve and location of sampled points.

configurations, a good alternative is based on sampling the Yield Ratio, $\mathrm{YR} = \frac{\mathrm{YS}}{\mathrm{UTS}} = \frac{R_p}{R_m}$ and fix a suitable lower bound on this quantity.

### 4.2. Strain-rate effect

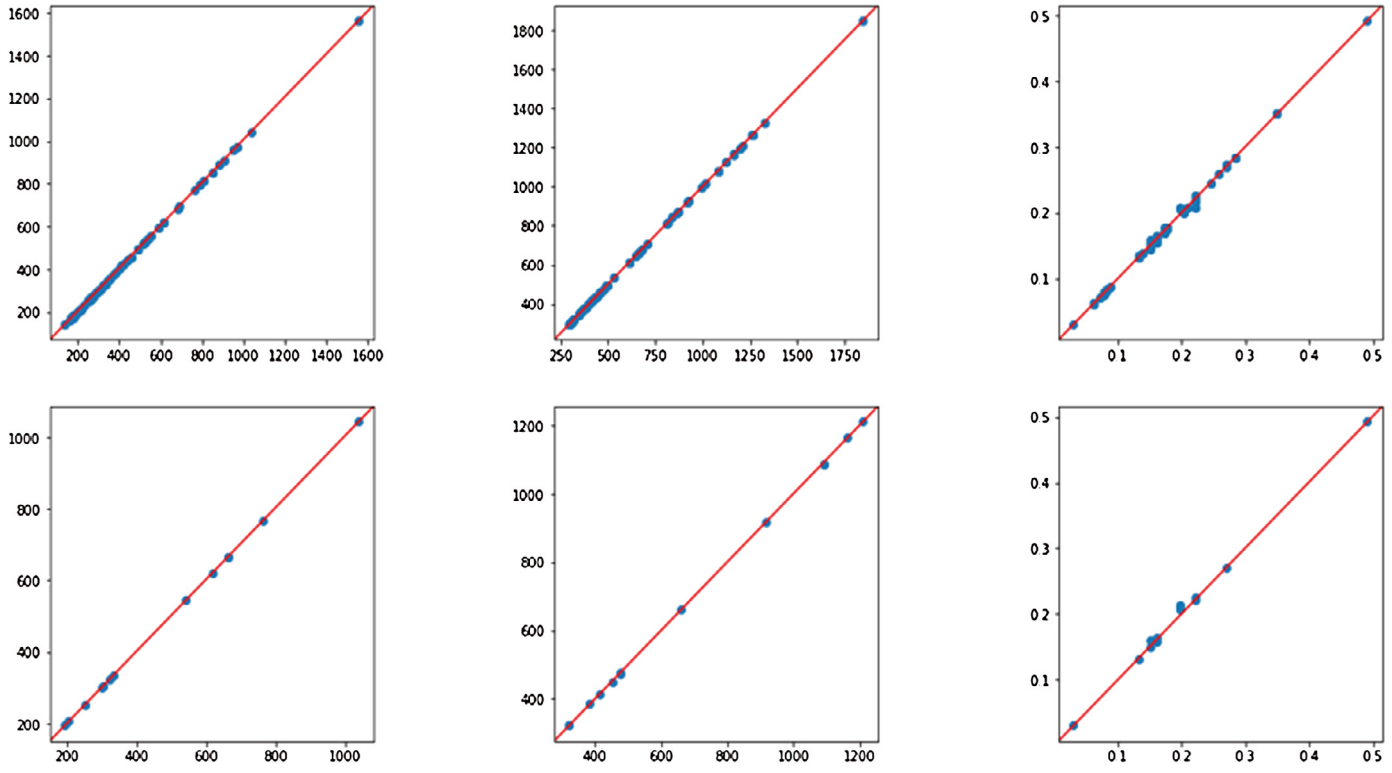
Since Strain-Rate Effect is considered in our simulations, the material of a part is identified by a rate-dependent plasticity curve (i.e., a plasticity curve for each rate). To correctly account for that in our parametric model, we exploit available experimental data collecting results of tests performed over specimens ranging from Mild Steel to Press Hardened Steel —PHS—. Such dataset links material properties

**Algorithm 1** Computation of Krupkowski plasticity parameters from material properties

**Input:** $R_p, R_m, A_g$
**Output:** $n, K, \varepsilon_0$

$A \leftarrow A_g/100$
$I \leftarrow A + 1$
$f(n) \leftarrow I\,R_m/R_p - (n/(n - \ln I))^n$
$n_0 \leftarrow 1.01 \ln I$
find $n$ such that $f(n) = 0$, given the initial guess $n_0$
▷ non-linear roots finder, e.g. Newton-Krylov optimization
$K \leftarrow R_p/(n - \ln I)^n$
$\varepsilon_0 \leftarrow n - \ln I$

observed at quasi-static test $(\mathrm{YS}, \mathrm{UTS}, \text{U-El})^{\mathrm{QS}}$ with the ones obtained at dynamic test under a strain rate $r$, $(\mathrm{YS}, \mathrm{UTS}, \text{U-El})^{\mathrm{D}}_r$. Each tuple of material properties identifies a plasticity curve, via Algorithm 1. For a given strain rate, we can therefore build a regression model whose features are the S-S curves at quasi-static test, while the targets are the corresponding S-S curves at dynamic test. Our data collect 1080 curves and account for 8 different strain rates $(0.008, 0.1, 1, 5, 10, 50, 100, 200)$ $\mathrm{s}^{-1}$, that is 135 curves for a given strain rate. Data observed at strain rate equal to 0.008 represent the quasi-static test. For each rate, a Single-layer Fully Connected Neural Network is trained (using a ReLU activation function), with a ratio between train and test data is set as 9:1. Moreover, a standardization based on the usual Min-Max scaler is used to normalize the input features prior to model fitting.



(a) YS [MPa]. (b) UTS [MPa]. (c) U-El [%].

**Fig. 13.** Predicted versus true values in case of rate 0.1; top: training data, bottom: test data.

Finally, for each part (Member-Front Side Outer, Member-Front Side Inner Front, Member-Front Side Inner Rear), the sampling procedure reads as follows:

1. sample $(\text{UTS}, \text{YR}, \text{U-El})^{\text{QS}}$, i.e. at strain rate 0.008 $\text{s}^{-1}$;
2. calculate YS from YR: $\text{YS} = \text{UTS} \cdot \text{YR}$;
3. for each rate $r$ in $(0.1, 1, 5, 10, 50, 100, 200)$ $\text{s}^{-1}$:
   (a) use the corresponding trained NN model to predict the tuple $(\text{YS}, \text{UTS}, \text{U-El})^{\text{D}}_r$ accounting for strain rate;
   (b) from the sampled tuple $(\text{YS}, \text{UTS}, \text{U-El})^{\text{D}}_r$, compute the corresponding plasticity parameters $(n, K, \varepsilon_0)_r$ via Algorithm 1 and, given the elongation $\varepsilon$, compute the curve $(\varepsilon, \sigma)_r$.
4. generate the material collecting the rate-dependent plasticity curves $(\varepsilon, \sigma)_r$.

For the sake of clarity, we underline that the Strain-Rate is not directly related to the Design of Experiments. After the sampling of a virtual material through its properties at quasi-static test, its response to Strain-Rate is predicted through the trained Neural-Networks models, allowing to obtain a plasticity curve for each rate characterizing such newly defined material.

Fig. 13 shows the results of NN predictions over train and test data, for Strain Rate 0.1. Table 3 gives the MSE values over train and test, which are small enough compared to the order of magnitude of the parameters.

Since the Strain-Rate —SR— models are trained over experimental data, one needs to pay special attention to point 1. Indeed, if the sampled virtual material is too far from the ones used for training the Neural-Network models, we cannot expect reliable Strain-Rate curve predictions (point 3). A standard Latin Hypercube Sampling would definitely not be a good approach, since the experimental data belong to a small manifold inside the hypercube. The sampling strategy we use is thus based on a $k$-nearest neighbors —KNN— algorithm and summarized in Algorithm 2, which allows us to move close to the training dataset without having to know the manifold to which the data belong (otherwise, one could investigate the data distribution through specific manifold learning techniques).

**Table 3.** MSE values for Neural-Network predictions.

| Strain Rate [$\text{s}^{-1}$] | YS [MPa] | | UTS [MPa] | | U-El [%] | |
|---|---|---|---|---|---|---|
| | Train | Test | Train | Test | Train | Test |
| 0.1 | 11.275 | 8.391 | 2.844 | 6.087 | $1.219 \cdot 10^{-5}$ | $5.318 \cdot 10^{-5}$ |
| 1 | 7.886 | 18.260 | 9.046 | 18.271 | $2.942 \cdot 10^{-5}$ | $2.937 \cdot 10^{-5}$ |
| 5 | 8.830 | 15.036 | 10.964 | 14.333 | $2.799 \cdot 10^{-5}$ | $3.743 \cdot 10^{-5}$ |
| 10 | 21.110 | 38.357 | 10.350 | 15.002 | $2.687 \cdot 10^{-5}$ | $2.757 \cdot 10^{-5}$ |
| 50 | 19.942 | 28.299 | 62.160 | 49.671 | $1.814 \cdot 10^{-5}$ | $2.015 \cdot 10^{-5}$ |
| 100 | 19.452 | 22.485 | 23.471 | 32.218 | $2.414 \cdot 10^{-5}$ | $3.319 \cdot 10^{-5}$ |
| 200 | 10.318 | 16.290 | 11.551 | 23.754 | $5.559 \cdot 10^{-6}$ | $5.116 \cdot 10^{-6}$ |

**Algorithm 2** KNN-based sampling of material properties

**Input:** number of points to be sampled $N$, number of neighbors $k$, experimental data $X \in \mathbb{R}^{M \times 3}$
**Output:** DoE
1: Apply a Min-Max scaling of data to obtain the normalized ones $X_{\text{adim}} \in [0, 1]^{M \times 3}$
2: Select randomly $N$ points from $X$ (i.e., $N$ random row indices)
3: **for** each selected point **do**
4: Find its $k$ nearest neighbors
5: Generate a new point as the linear combination of such $k$ neighbors (with random weights)
6: Add the newly generated point to the DoE
7: **end for**

### 4.3. Parametric metamodel construction

The new parametric model accounts for 13 parameters, as reported in Table 4 and sketched in Fig. 14. The three steel parts (Member-Front Side Outer, Member-Front Side Inner Front, Member-Front Side Inner Rear) have parametric material properties and thickness, while the Crash Boxes have only parametric thickness. 70 Hi-Fi simulations

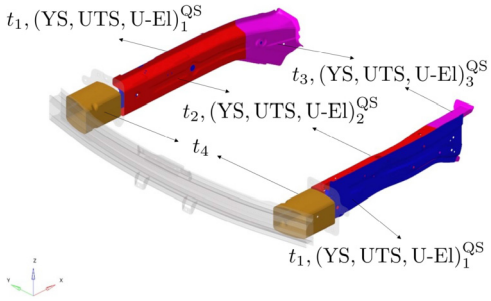
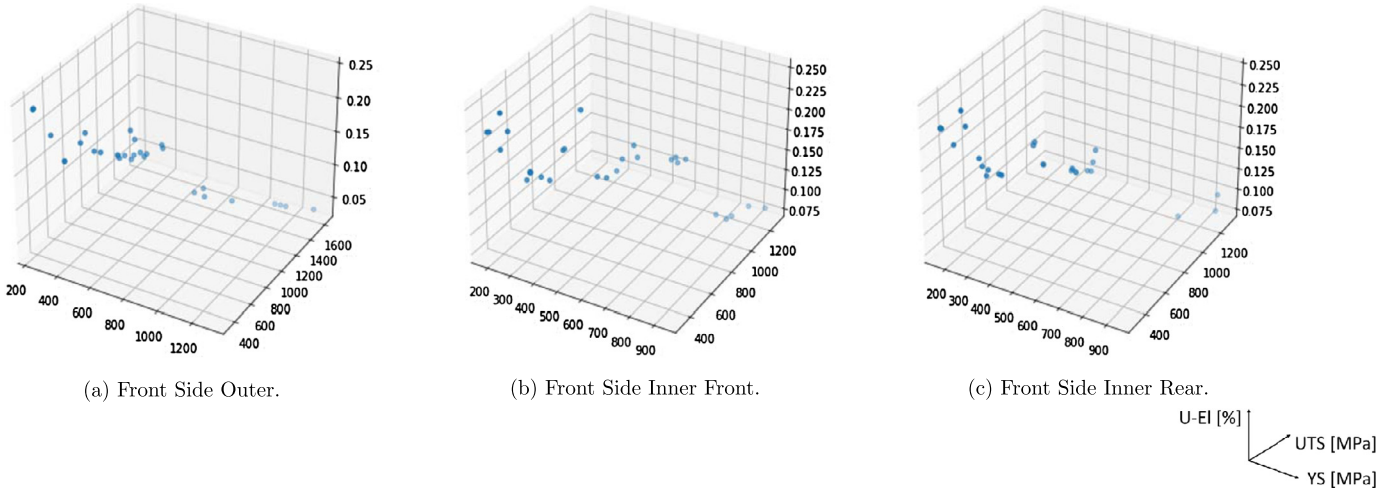
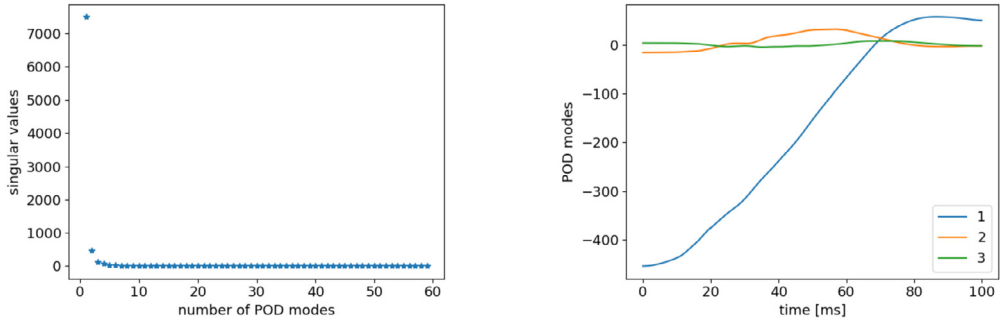



**Fig. 14.** Sketch of parts with parametric thickness and material properties.




(a) Front Side Outer. (b) Front Side Inner Front. (c) Front Side Inner Rear.

**Fig. 15.** 30 sampled points $(\text{YS}, \text{UTS}, \text{U-El})^{\text{QS}}$ using the KNN-based algorithm.




(a) Decay of singular values. (b) Selected modes.

**Fig. 16.** POD results for LH $x$-velocity snapshots.

**Table 4.** DoE structure for thickness $t$ and material parameters $(\text{YS}, \text{UTS}, \text{U-El})^{\text{QS}}$.

| Outer | | Inner Front | | Inner Rear | | Crash Box |
|---|---|---|---|---|---|---|
| $t_1$ | $(\text{YS}, \text{UTS}, \text{U-El})_1^{\text{QS}}$ | $t_2$ | $(\text{YS}, \text{UTS}, \text{U-El})_2^{\text{QS}}$ | $t_3$ | $(\text{YS}, \text{UTS}, \text{U-El})_3^{\text{QS}}$ | $t_4$ |

**Table 5.** $L^2$ norm relative errors on test.

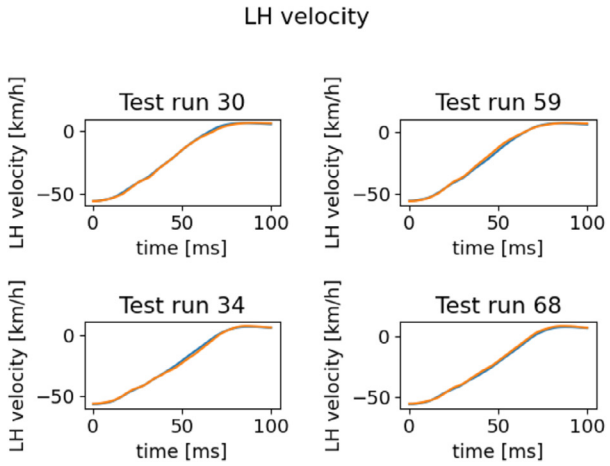
| Run 30 | | Run 59 | | Run 34 | | Run 68 | |
|---|---|---|---|---|---|---|---|
| LH | RH | LH | RH | LH | RH | LH | RH |
| 0.023 | 0.023 | 0.036 | 0.033 | 0.014 | 0.029 | 0.033 | 0.023 |

have been performed, 66 are taken for training the model while remaining 4 for validation.

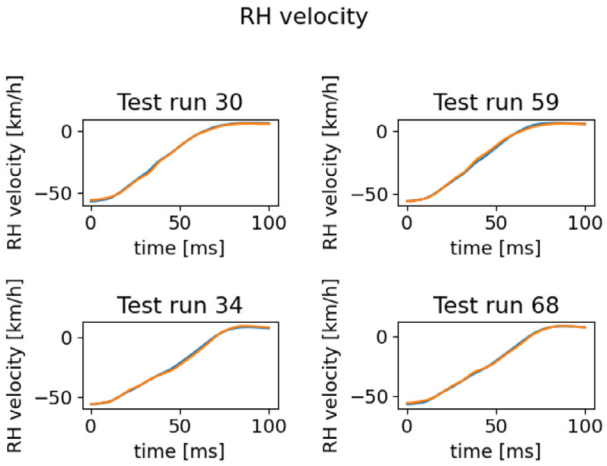
The parameter range for thicknesses is the same as the introductory study of Section 3, reported in Table 1. Material properties at quasi-static test have been sampled via the KNN-based Algorithm 2 and, according to the available experimental data, they range from Mild Steel to Press Hardened Steel. Fig. 15 shows, for instance, 30 sampled points using this procedure, for the three parts. The material properties for one simulation are $\text{MAT}_{\mathcal{P}} = (\text{YS}, \text{UTS}, \text{U-El})_{\mathcal{P}}^{\text{QS}}$, with $\mathcal{P} = 1, 2, 3$ the corresponding part, meaning in total 9 material parameters. Such parameters are obtained taking the sampled point in the three 3D plots of Fig. 15 simultaneously. From the points sampled at quasi-static test, we can compute the parameters accounting for strain rate by means of the trained Neural-Network, as detailed in Subsection 4.2.

Analyzing the singular values pattern, we deduce that three modes contain the most information. For instance, Fig. 16 shows the POD results in the case of velocity computed at the left-side of the vehicle (LH). The sPGD regression is thus applied as described in the previous section.

Fig. 17 shows the plots of predicted curves for testing points and Table 5 gives the related $L^2$ norm relative errors.

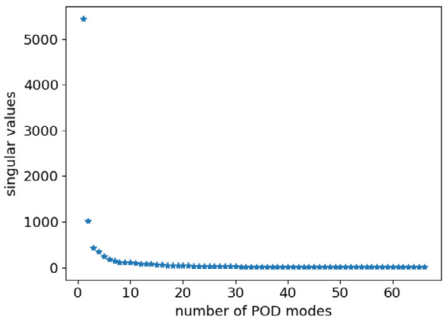



(a) Velocity at LH measurement point.

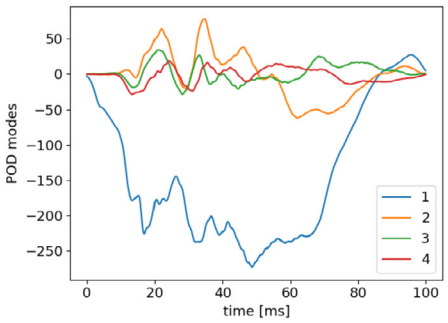



(b) Velocity at RH measurement point.

**Fig. 17.** Reconstructed $x$-velocity using the sPGD models (orange: Hi-Fi simulation, blue: Reduced Model).

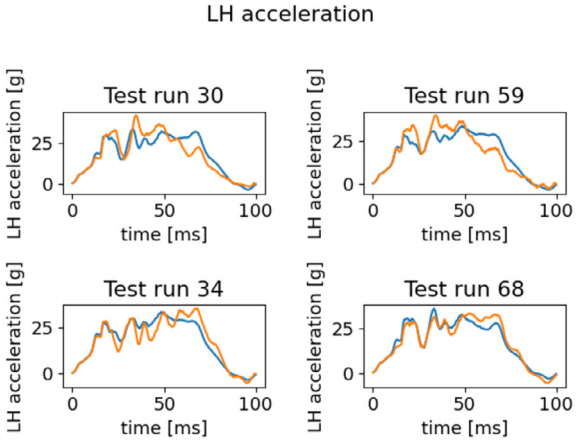



(a) Decay of singular values.

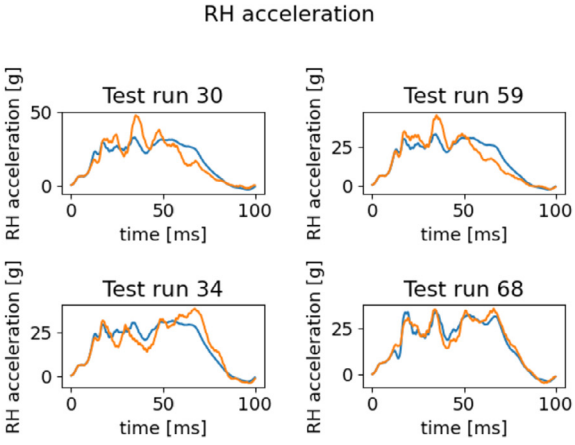



(b) Selected modes.

**Fig. 18.** POD results for LH $x$-acceleration snapshots.




(a) Acceleration at LH measurement point.




(b) Acceleration at RH measurement point.

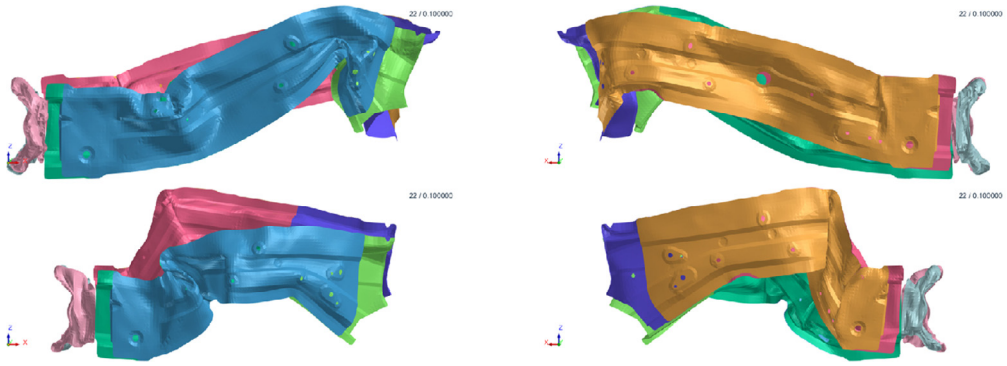
**Fig. 19.** Reconstructed $x$-acceleration using the sPGD models (orange: Hi-Fi simulation, blue: Reduced Model).

The same study is done over acceleration curves, for which first four modes are selected after a scaling analysis on singular values (see Fig. 18).

In Fig. 19 predictions on acceleration curves are given. Regardless a well captured global shape, the oscillations and peaks amplitudes characterizing the transitory regimen are mostly wrong. One can notice that in runs 30 and 59 the measurement node starts decelerating at almost 45 ms. Different behavior is observed for runs 34 and 68 where the point keeps accelerating up to almost 65 ms and suddenly decelerates with a more pronounced slope. Such simulations highlight substantially different crash dynamics. The low accuracy of predictions can thus be ascribed to a model which is mixing and averaging such dynamics. These comments motivate the clustering-based approach investigated in the next section.

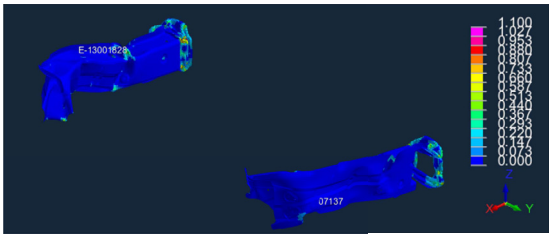
## 5. Multi-PGD

Further improvements can be reached through the multi-regression strategy briefly discussed in Section 2.4 of [10]. The idea is basically to cluster the high-fidelity simulations according to the most relevant

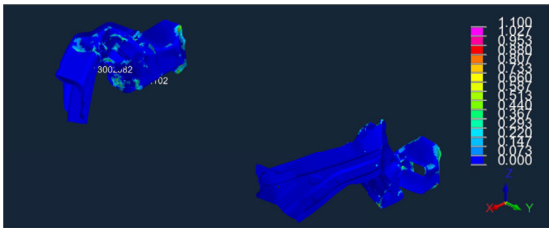


(a) Left-side view. (b) Right-side view.

**Fig. 20.** Two different crash modes, at bottom and top. Snapshots taken at the last timestep.



(a) Crash mode 1.



(b) Crash mode 2.

**Fig. 21.** Two different crash modes (plastic-strain over the deformed structure with isometric view). Snapshots taken at the last timestep.

crash mode, e.g. buckling and compression behaviors, as emphasized in Figs. 20 and 21. Once a cluster criterion is established, separate reduced models are built. A classification algorithm is also necessary since, during the online phase, one needs to identify the right cluster for a new simulation (coming for a new choice of parameters).

### 5.1. Clustering

The approach followed in this work is based on clustering the high-fidelity simulations according to the displacement of lower boundary nodes of the left side member as illustrated in Fig. 22. A similar clustering procedure was also applied in [14].

**Table 6.** Configuration of parameters for base mode definition.

| Outer | | Inner Front | | Inner Rear | | Crash Box |
|---|---|---|---|---|---|---|
| 1.4 | SPFC980Y | 1.8 | SPFC590DP | 2 | SPFC590DP | 3.2 |

First, a reference deformation mode is computed for a specific configuration of parameters, reported in Table 6 (same layout as Table 4).

Then, for each simulation we compute the mean distance of its lower boundary nodes to such reference mode (each coordinate $x$, $y$ and $z$ separately) and use a min-max scaling to normalize data. In such a way, a unique point in three-dimensional space is associated to each simulation. A hierarchical cluster based on ward linkage and euclidean affinity is applied and two clusters are obtained, as shown in Fig. 23.

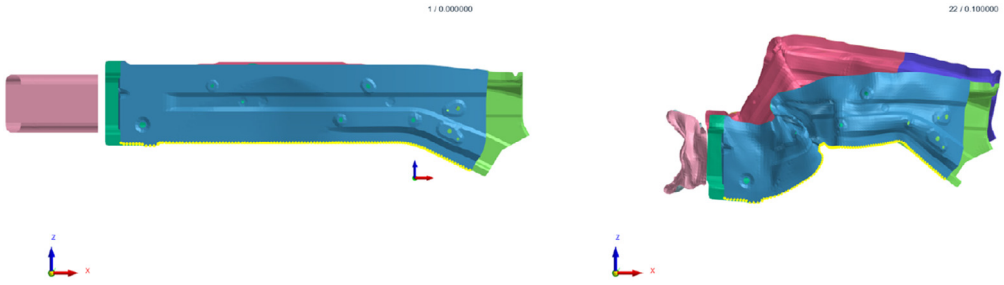
Fig. 24 shows an important difference in final deformation stage between the two clusters (up and down parts of the figure).

### 5.2. Multi-regression models

In Figs. 25 and 26 we give the results of POD performed separately for each cluster, for left and right measurement points, respectively. As remarked at the end of Section 4, the two clusters identified based on the crash dynamics influence the final part of the acceleration curve (starting from 45 ms). In the first scenario, the measurement node starts decelerating while in the second one it keeps accelerating up to a maximum point (at almost 65 ms) and then suddenly falls. Two sPGD models are thus trained and calibrated, one for each cluster.

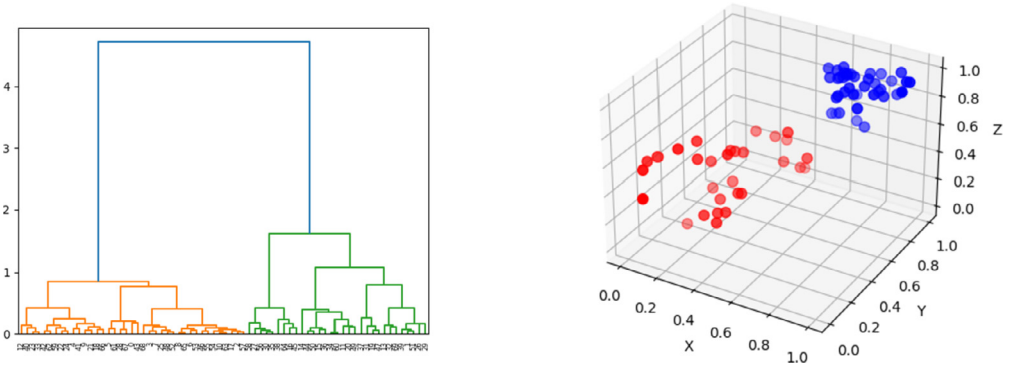
### 5.3. Classification

A classification step shall also be integrated in the procedure since, for a new choice of parameters, one must be able to select the right submodel for curves prediction. A Random Forest classifier was employed for this study, whose confusion matrix is given in Fig. 27.



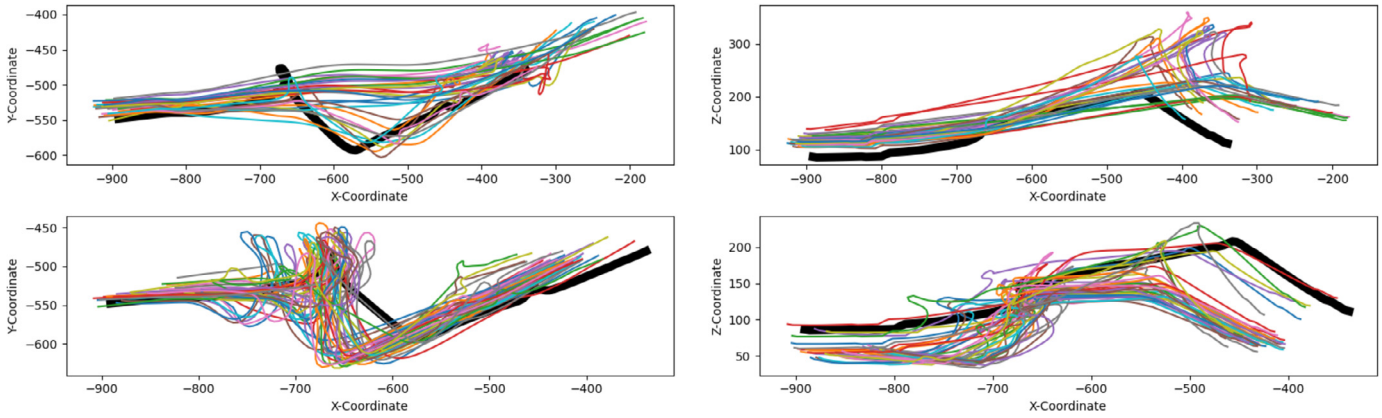
(a) Initial state. (b) Final state.

**Fig. 22.** Left side member lower boundary displacement. Nodes of interest are highlighted in yellow.



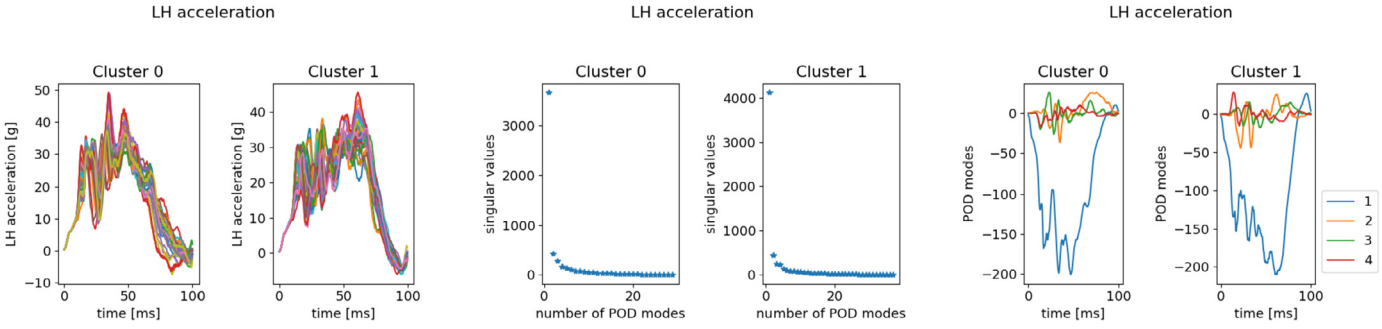

(a) Dendrogram of agglomerative cluster. (b) Labeled data points.

**Fig. 23.** Hierarchical clustering results.



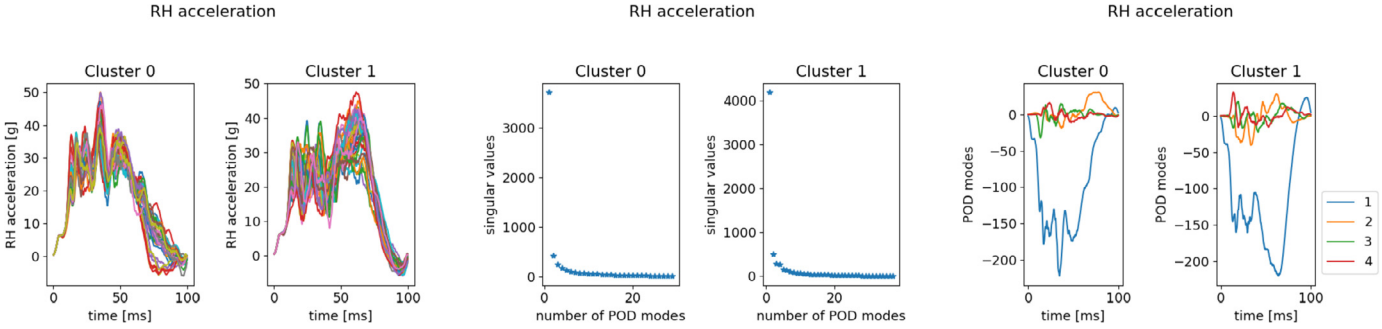

(a) $y$ coordinate versus $x$ coordinate. (b) $z$ coordinate versus $x$ coordinate.

**Fig. 24.** Two clustered deformation modes (up and down); black fat line representing the reference mode.




(a) Curves snapshots. (b) Decay of singular values. (c) Selected modes.

**Fig. 25.** POD results for LH $x$-acceleration snapshots within the two identified clusters.




(a) Curves snapshots. (b) Decay of singular values. (c) Selected modes.

**Fig. 26.** POD results for RH $x$-acceleration snapshots within the two identified clusters.

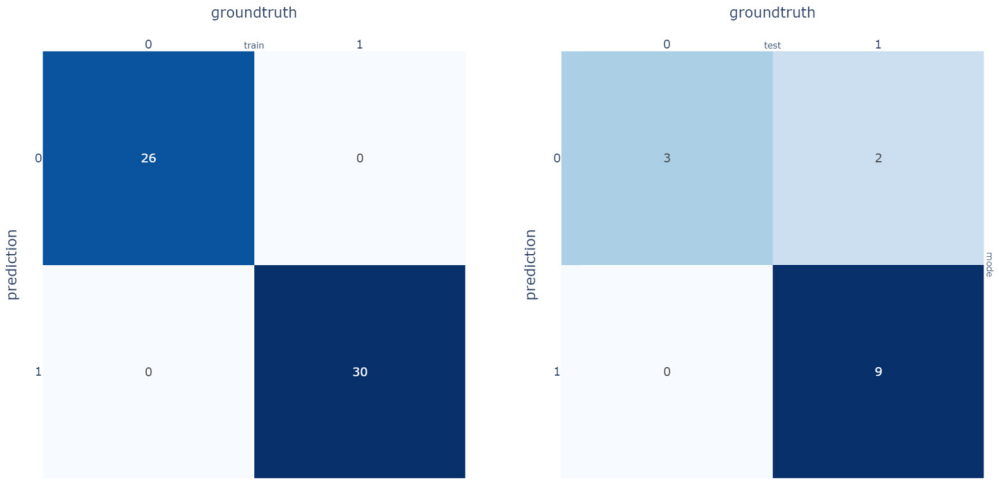
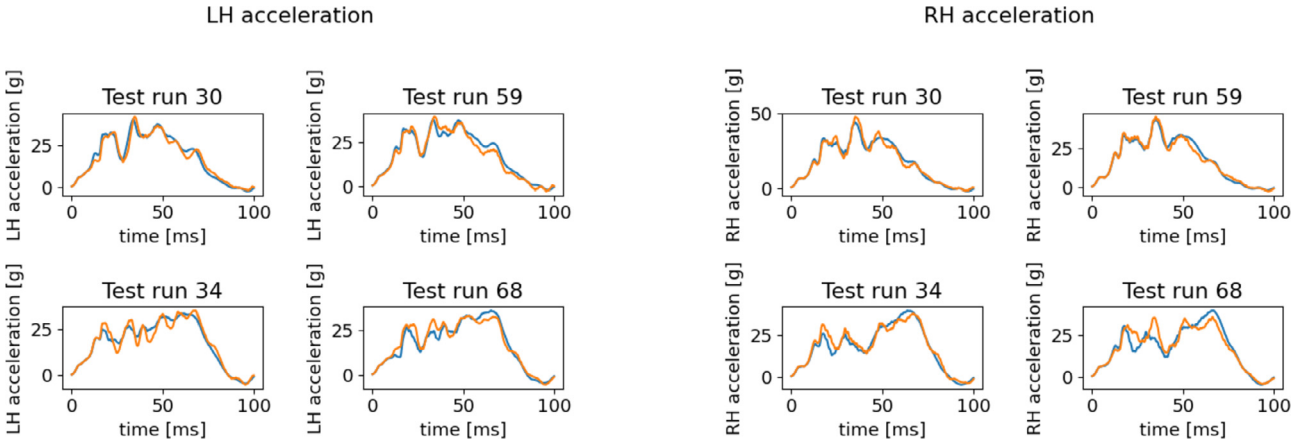



**Fig. 27.** Confusion matrix for Random Forest Classifier.




(a) Acceleration at LH measurement point.

(b) Acceleration at RH measurement point.

**Fig. 28.** Reconstructed $x$-acceleration using the multi-PGD models (orange: Hi-Fi simulation, blue: Reduced Model).

Finally, in Fig. 28 we give the results on the acceleration predictions. As expected, test runs 30 and 59 belong to the first cluster, while 34 and 68 to the second one.

The first peak and the final part of the curve are now almost perfectly predicted. The average $L^2$ norm error is now reduced to 9% on average, against the 15% of the unique model.

## 6. Conclusion, further developments and applications

In the present study a parametric model of the vehicle frontal structure has been built and numerically tested over a full-frontal crash. Thicknesses and material properties of the front side members are parametric.

Virtual plastic materials can be sampled moving near the manifold identified by experimental data collected for the quasi-static material tests. The rate-dependent Krupkowski plasticity curves (i.e., the strain-rate effects) are consequently built according to trained Neural-Network models linking experiments at quasi-static and dynamic tests. The Neural Networks show great accuracy in the prediction from quasi-static to dynamic, meaning that the parametric strain-rate is of great precision.

The model allows to evaluate in real time the influence of 13 parameters (4 thicknesses and 9 material properties), without needs of performing again a full vehicle crash computation. To improve the accuracy of acceleration curves predictions a hierarchical clustering on crash dynamics has been performed and separate multi-regression models have been built. Accordingly, a Random Forest classifier is trained to identify the right cluster for a newly defined run.

Although the accuracy of the model seems to be really satisfactory considering its computational gains, several developments could be attempted for accuracy improvements. First, a reduced parametric space could be considered, being the material parameters range quite wide in this study (from Mild Steel to Press Hardened Steel). Some other strategies, towards specific and physics-informed models, will also be part of our future research in this line. The curves could, indeed, be split in several regimes and separate sub-models could be built for each part of the curve. For this, one could be inspired by the curves alignment methodology proposed in [10]. Such regimes are often evident observing the acceleration-displacement curve and its integral function (RDE as a function of the displacement). Once the different regimes identified, some physical considerations could be embedded in the model to understand which parameters are actively influencing a specific part of the curve. For instance, since in the energy absorption the crash boxes act before then the side members, the parameters of crash boxes shall influence mostly the first part of the pulse. Similarly, the transitory part will mostly be influenced by side members parameters.

Among the applications and advantages of the proposed procedure, there is the monitoring, in real time, of the influence of material parameters on all safety indices like RDE, OLC, first peak acceleration or rebound time. Moreover, defining a parametric metamodel for another crash scenario, e.g. an offset crash, a constrained optimization problem could be considered: find the optimal parameters to minimize

the frontal structure weight or manufacturing cost while respecting all crash performance specifications. We may also comment-out about the design space. In this paper, only the frontal structure has been parametrized. However, in our works in progress, we focus also on models where several parts (in the whole vehicle) are parametric and where the reduced-order model is built for all the measured 3D fields. In general, higher the number of parameters, higher the number of required high-fidelity simulations. Although this is a classical limitation of Non-Intrusive ROMs —NI-ROMs—, the sPGD structure allows us to work in the low-data limit even in high-dimensional parametric spaces. The algorithm, as done in this paper, needs sometimes, for the sake of accuracy, to be coupled with fields alignment, clustering and classification. This requires, not only good results from the clustering step, but also the existence of a discriminant in the design space and a classifier able to detect it. From clustering and classification results obtained in [10] and in this work, the multi-sPGD seems being really promising. In our current research we are focusing on developing new methodologies based on a non-intrusive parametric domain-decomposition approach to reduce the computational effort required when many parts (consequently, many parameters) are involved.

## Declarations

### *Author contribution statement*

Angelo Pasquale, Victor Champaney: Conceived and designed the experiments; Performed the experiments; Analyzed and interpreted the data; Wrote the paper.

Youngtae Kim: Performed the experiments; Analyzed and interpreted the data.

Nicolas Hascoët, Amine Ammar, Francisco Chinesta: Contributed reagents, materials, analysis tools or data.

### *Funding statement*

This research did not receive any specific grant from funding agencies in the public, commercial, or not-for-profit sectors.

### *Data availability statement*

The data that has been used is confidential.

### *Declaration of interests statement*

The authors declare no conflict of interest.

### *Additional information*

No additional information is available for this paper.

## Acknowledgements

The authors acknowledge the support of ESI Group through its International Research Chair CREATE-ID at ENSAM ParisTech.

Sincere gratitude is extended by the authors to Engineer Junhyung Kim (ESI Group, Hybrid Twin Team – South Korea area) for his contribution to this work.

## References

[1] P. Benner, et al., Model Order Reduction: System- and Data-Driven Methods and Algorithms, De Gruyter, Berlin, 2020.
[2] P. Benner, et al., Model Order Reduction: Snapshot-Based Methods and Algorithms, De Gruyter, Berlin, 2020.
[3] P. Benner, et al., Model Order Reduction: Applications, De Gruyter, Berlin, 2020.
[4] Domenico Borzacchiello, Jose V. Aguado, Francisco Chinesta, Non-intrusive sparse subspace learning for parametrized problems, Arch. Comput. Methods Eng. 26 (July 2017).
[5] Francisco Chinesta, et al., PGD-based computational Vademecum for efficient design, optimization and control, Arch. Comput. Methods Eng. 20 (Mar. 2013).
[6] Francisco Chinesta, Roland Keunings, Adrien Leygue, The Proper Generalized Decomposition for Advanced Numerical Simulations. A Primer, Jan. 2014.
[7] Model reduction methods, in: Encyclopedia of Computational Mechanics, second edition, John Wiley & Sons, 2017, pp. 1–36.
[8] Rubén Ibáñez Pinillo, et al., A multidimensional data-driven sparse identification technique: the sparse proper generalized decomposition, Complexity 2018 (Nov. 2018) 1–11.
[9] Rubén Ibáñez Pinillo, et al., A local, multiple proper generalized decomposition based on the partition of unity, Int. J. Numer. Methods Eng. 120 (May 2019).
[10] Victor Champaney, et al., Parametric curves metamodelling based on data clustering, data alignment, POD-based modes extraction and PGD-based nonlinear regressions, Front. Mater. (ISSN 2296-8016) 9 (2022), https://www.frontiersin.org/article/10.3389/fmats.2022.904707.
[11] Francisco Chinesta, Elías Cueto, Simon Guévelou, Material forming digital twins: the alliance between physics-based and data-driven models, Key Eng. Mater. 926 (July 2022) 3–14.
[12] Francisco Chinesta, Elias Cueto, Empowering engineering with data, machine learning and artificial intelligence: a short introductive review, Adv. Model. Simul. Eng. Sci. 9 (Oct. 2022) 21.
[13] Kai Liu, Duane Detwiler, Andres Tovar, Metamodel-based global optimization of vehicle structures for crashworthiness supported by clustering methods, in: Axel Schumacher, et al. (Eds.), Advances in Structural and Multidisciplinary Optimization, Springer International Publishing, Cham, 2018, pp. 1545–1557.
[14] S. Hashimoto, et al., Development of prediction method by reduced model for structural deformations in frontal impact, Trans. Soc. Automot. Eng. Jpn. 50 (2019) 1102–1107.
[15] Yves Le Guennec, et al., A parametric and non-intrusive reduced order model of car crash simulation, Comput. Methods Appl. Mech. Eng. 338 (Mar. 2018).
[16] C.-K. Park, C.-D. Kan, Objective evaluation method of vehicle crash pulse severity in frontal new car assessment program (NCAP) tests, in: 24th Int. Technical Conf. Enhanced Safety of Vehicles (ESV), 2015.
[17] C. Park, C. Kan, A Study on Vehicle Crash Pulse Severity in Frontal NCAP Tests, SAE Technical Paper 2016-01-1536, 2016.
[18] L. Kübler, S. Gargallo, K. Elsäßer, Frontal crash pulse assessment with application to occupant safety, ATZ Worldw. 111 (6) (2009) 12–17.
[19] V. Sandner, J. Ellway, M. van Ratingen, New frontal impact test with mobile progressive deformable barrier (MPDB), in: Euro NCAP, 2019.
[20] Shaobo Qiu, et al., Optimized Ride-Down Rate Control in Frontal Impact and its Application in the Energy Management of Occupant Restraint System, Apr. 2013.
[21] H. Katoh, R. Nakahama, A study on the ride-down evaluation proceeding, in: 9th International Conference on Experimental Safely Vehicles, 1982.
[22] N. Evans, L. Furton, D. Cok, Occupant Energy Management Technique for Restrain System analysis and Design-Theory and Validation, SAE Technical Paper 922082, 1992.
[23] M. Huang, J. Laya, M. Loo, A Study on Ride-Down Efficiency and Occupant Responses in High Speed Crash Tests, SAE Technical Paper 950656, 1995.